

1 Resolving the role of carbonaceous material in gold  
2 precipitation in metasediment-hosted orogenic gold  
3 deposits

4 Si-Yu Hu<sup>1,2</sup>, Katy Evans<sup>1</sup>, Dave Craw<sup>3</sup>, Kirsten Rempel<sup>1</sup>, and Kliti Grice<sup>2</sup>

5 <sup>1</sup>*Department of Applied Geology, Curtin University, GPO Box U1987, Perth, WA 6845,*  
6 *Australia*

7 <sup>2</sup>*Western Australia Organic and Isotope Geochemistry Centre, Department of Chemistry,*  
8 *Institute for Geoscience Research, Curtin University, GPO Box U1987, Perth, WA 6845,*  
9 *Australia*

10 <sup>3</sup>*Geology Department, University of Otago, GPO Box 56, Dunedin 9054, New Zealand*

11 **ABSTRACT**

12 Carbonaceous material (CM) is commonly associated with gold and sulfides in  
13 metasediment-hosted orogenic gold deposits. The role of CM in Au deposition is  
14 controversial; CM has been proposed to contribute to gold deposition by reducing Au  
15 bisulfide complexes, or by facilitating sulfidation, which destabilizes Au in bisulfide  
16 complexes with resultant Au deposition. Integration of petrographic observations,  
17 thermodynamic models, and geochemical data from metasediment-hosted orogenic gold  
18 deposits in New Zealand, Australia, Canada, and West Africa reveals genetic links  
19 between sulfides, CM, and mineralization. The results are consistent with the coexistence  
20 of CM and pyrite as a consequence of their codeposition from ore fluids, with a minor  
21 proportion of CM originally in situ in the host rocks. Au is deposited when pyrite and  
22 CM deposition decreases H<sub>2</sub>S concentration in ore fluids, destabilizing Au(HS)<sub>2</sub><sup>-</sup>

23 complexes. Most CM in gold deposits is deposited from CO<sub>2</sub> and CH<sub>4</sub> in ore fluids.

24 These findings are applicable to similar deposits worldwide.

## 25 INTRODUCTION

26 Metasediment-hosted orogenic gold deposits such as the Victorian goldfields of  
27 Australia (Bierlein et al., 2001), the Macraes gold deposit of New Zealand (Craw, 2002),  
28 and the Paleoproterozoic gold deposits of West Africa (Křibek et al., 2015) are some of  
29 the world's largest. As with most orogenic gold deposits, ore fluids are low salinity, CO<sub>2</sub>  
30 rich, often CH<sub>4</sub> bearing, with pH near-neutral, and are proposed to have been generated  
31 during the lower greenschist to amphibolite facies transition (Berge, 2011; De Ronde et  
32 al., 2000; Goldfarb and Groves, 2015; Tomkins, 2010). Gold in metasediment-hosted  
33 orogenic gold deposits is proposed to be sourced from organic, pyrite-rich sediments (Hu  
34 et al., 2016; Large et al., 2011; Pitcairn et al., 2006; Thomas et al., 2011). Mineralization  
35 commonly occurs in shear zones at pressures of 1–3 kbar and temperatures of 200–400  
36 °C. In auriferous zones, carbonaceous material (CM) is widespread and spatially  
37 associated with gold and sulfides (Berge, 2011; Bierlein et al., 2001; Craw et al., 2015;  
38 Hu et al., 2015; Křibek et al., 2015). CM may be in situ, derived from organic matter that  
39 was deposited with the sediments and matured during metamorphism (Berge, 2011;  
40 Bierlein et al., 2001). Alternatively, CM may be deposited from hydrothermal fluids  
41 (Křibek et al., 2015; Pitcairn et al., 2005). CM has long been thought to contribute to gold  
42 deposition, but the role of CM is not well understood. Possible roles for CM were  
43 summarized in Hu et al. (2015).

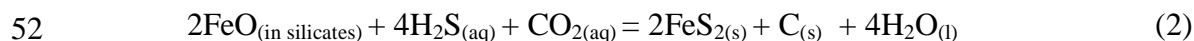
44 1. In situ CM reduces Au in solution to cause gold precipitation via Reaction 1: 45



46 where aq is aqueous (e.g., Cox et al., 1995).

47 2. Hydrothermal CM deposited prior to mineralization acts as a reductant via  
48 Reaction 1.

49 3. Hydrothermal CM precipitates from fluids with sulfides via Reaction 2; loss of  
50 sulfur from solution drives Au deposition via destabilization of aqueous Au-sulfide  
51 complexes:



53 (modified from Craw et al., 2015).

54 4. CM plays a physical role in Au precipitation by facilitating the formation of  
55 shear zones that focus fluid flow (e.g., Upton and Craw, 2008).

56 In this study we combine thermodynamic modeling using the HCh software  
57 package (Shvarov and Bastrakov, 1999) with new petrographic observations and  
58 geochemical analyses of samples from the Macraes gold deposit, New Zealand, and with  
59 published geochemical data from similar gold deposits to test these hypotheses. We use  
60 Macraes as the primary example because of the availability of an extensive data set and  
61 abundant CM in mineralized rocks (Craw, 2002). However, the results are relevant to  
62 other similar gold deposits where CM is ubiquitous (e.g., Křibek et al., 2015).

### 63 **PETROGRAPHIC OBSERVATIONS**

64 In the Macraes deposit, CM, sulfides, and Au are spatially associated in  
65 mineralized rocks. CM is dominantly hydrothermal, introduced during mineralization,  
66 exhibiting flat spectra of typical graphite in Fourier transform infrared spectroscopy  
67 (FTIR) analysis, although some matured in situ CM showing kerogen FTIR spectra also  
68 occurs in the host rocks (Craw, 2002; Henne and Craw, 2012; Hu et al., 2015; Pitcairn et

69 al., 2005). Gold occurs primarily as microscale inclusions in sulfides (Petrie et al., 2005).  
70 Textural analysis suggests that auriferous sulfides are texturally synchronous with, or  
71 after the formation of, graphitic microsphaeres that include fine-grained CM and sulfides  
72 (Fig. 1; Craw, 2002; Upton and Craw, 2008).

### 73 **SAMPLES AND METHODS**

74 Mineralized rocks from the Golden Bar pit in the Macraes deposit were analyzed  
75 for sulfur (S) and noncarbonate carbon (NCC). Methods were described in Hu et al.  
76 (2015, 2016). Additional S and NCC data for mineralized and unmineralized rocks in the  
77 Macraes deposit were collected using X-ray fluorescence at the University of Otago, New  
78 Zealand (Craw, 2002). Previously unpublished data are listed in Table DR2 in the GSA  
79 Data Repository<sup>1</sup>. Extant S and NCC data were obtained from the Victorian goldfield  
80 (Australia; Bierlein et al., 2001), the Touquoy Zone deposit (Meguma terrane, Canada;  
81 Bierlein and Smith, 2003), several Paleoproterozoic deposits (West Africa; Křibek et al.,  
82 2015), and other Macraes mine pits (Craw, 2002; Petrie et al., 2005). These published  
83 data are listed in Table DR3.

84 The HCh program coupled with the Unitherm database was used for  
85 thermodynamic modeling (Shvarov and Bastrakov, 1999). Bulk-rock compositions used  
86 in the modeling were derived from Otago Schist and Golden Bar pit samples (Hu et al.,  
87 2015). The chemical components of the systems investigated are Al<sub>2</sub>O<sub>3</sub>-CaO-CuO-K<sub>2</sub>O-  
88 FeO-MgO-Na<sub>2</sub>O-SiO<sub>2</sub>-ZnO-Au-As-C-CO<sub>2</sub>-S-H<sub>2</sub>O. The conceptual model was designed  
89 to simulate infiltration of ore fluids generated by underlying metasediments into lower  
90 greenschist facies rocks, a process proposed to apply to the Macraes deposit and other  
91 similar CM-rich gold deposits (Pitcairn et al., 2006; Large et al., 2011).

92 Production of the ore fluid by equilibration of metamorphic fluids with a  
93 sedimentary host rock at depth was simulated in an initial model cell in which an H<sub>2</sub>O-  
94 rich fluid (fluid 1) was equilibrated with a graphite- and Au-bearing rock at 500 °C and 5  
95 kbar. The rock composition was that of a CM-rich sample (FF-13) from the prehnite-  
96 pumpellyite facies and is thought to be typical of the source rocks (Hu et al., 2016).  
97 Magnetite, pyrrhotite, and pyrite were set in excess in this initial cell to simulate fluid  
98 production under  $f_{O_2} - f_{S_2}$  (oxygen and sulfur fugacity, respectively) conditions  
99 representative of the greenschist-amphibolite transition. Details of fluid 1 and FF-13 rock  
100 compositions are provided in Table DR1.

101 Subsequent model cells were designed to simulate spatial variation in fluid-rock  
102 interaction during ore fluid infiltration into lower greenschist metasediments. The  
103 composition of these rocks was based on that of a Golden Bar pit sample (GB-01; Table  
104 DR1). In the model, the ore fluid infiltrates a notional cell containing GB-01 at 3 kbar  
105 and a specified mineralization temperature ( $T_{min}$ ). After equilibration of the ore fluid with  
106 the rock in that cell at  $T_{min}$ , the fluid was passed to the next cell at the same pressure and at  
107  $T_{min}$ , where it was equilibrated and passed on again. The first cell of this model, where the  
108 ore fluids are added to the host rock at  $T_{min}$ , simulates the addition of channelized fluid to  
109 a host rock with which the fluid is not in thermal or chemical equilibrium. Subsequent  
110 cells simulate slower pervasive isothermal and isobaric infiltration of the fluid into the  
111 surrounding country rock. Infiltration at 160–400 °C was investigated to assess the  
112 effects of fluid infiltration at different levels in the crust (Table DR4).

113 The integrated fluid:rock ratio for each simulation was 1:1 by mass. Simulations  
114 were run to assess the effects of adding this fluid in different numbers of increments,

115 from 1 to 20, i.e., with instantaneous fluid:rock ratios between 0.05 and 1. Changes in the  
116 instantaneous fluid:rock ratio did not affect the conclusions (Table DR5). Phase  
117 separation was neglected because there is no evidence of phase separation reported from  
118 Macraes (De Ronde et al., 2000). The dependence of our conclusions on the assumption  
119 that the fluid did not reequilibrate between the source and the host rock was also tested by  
120 running a model in which the fluid was reequilibrated at  $T_{\min}$  (e.g., 220 °C) and 3 kbar  
121 prior to infiltration into the host rock. The results from this alternative model are  
122 consistent with those presented here (Table DR6).

123         The results for 14 cells are presented here because this number was sufficient to  
124 reproduce the mineralogical zoning observed in the field. Note that the bulk composition  
125 of GB-01 was set such that fluid was present in the host rock (fluid:rock = 0.025 by  
126 mass) prior to ore fluid infiltration. Equilibration between the ore fluid and the country  
127 rock thus involves mixing between the country-rock fluid and the infiltrating fluid, as  
128 well as reaction between the infiltrating fluid and the host rock. It was therefore  
129 necessary to include the host-rock fluid in calculations of species concentration changes  
130 during reaction. Changes in species concentrations were calculated for each cell by  
131 comparing the concentrations of the species of interest in the unreacted mixture with  
132 those in the equilibrated products.

133         CM abundance is reported as NCC for natural samples and  $C_{\text{model}}$  for modeled  
134 graphite. In reality, CM in natural samples is not pure graphite, but a complex mixture of  
135 C-O-H compounds that are difficult to characterize and currently impossible to model.  
136 Representation of CM by graphite in the model introduces uncertainty, but primary  
137 trends are considered robust because CM will respond

138 to external changes in pressure, temperature, and redox in a way similar to graphite.

139 Whole-rock sulfur concentration is referred to as S for natural samples and  $S_{\text{model}}$  for  
140 modeling results.

## 141 RESULTS

### 142 Geochemical Analyses

143 In unmineralized rocks, the S and NCC contents are generally <1 wt% (Fig. 2).

144 The data in mineralized rocks show considerable scatter, but the S and NCC contents  
145 range to values ~10 times higher than those in unmineralized rocks (Fig. 2).

### 146 Thermodynamic Modeling

147 Calculated mineral assemblages in the mineralized rock are consistent with those  
148 observed in the field, comprising graphite, quartz, pyrite, arsenopyrite, calcite, siderite,  
149 muscovite, epidote, chlorite, and albite. Infiltration at different temperatures produced  
150 assemblages compatible with known phase stability fields (Table DR4). Pyrite and  
151 arsenopyrite are predicted to coexist at temperatures <310 °C.

152 Typical model results for 220 °C, 3 kbar are shown in Figure 3. Deposition of Au,  
153 sulfides, and graphite occurs in all cells, but primarily in the first infiltration cell (Fig. 3).  
154 Pyrrhotite is stable in the unaltered model host rock, consistent with Pitcairn et al. (2006),  
155 but pyrite is the dominant sulfide in infiltrated rocks (Fig. 3A). In unaltered rocks at  
156 Macraes, As is present as arsenian pyrite, which cannot be accommodated by the model.  
157 Therefore, calculated arsenopyrite is reasonable. Additional arsenopyrite is predicted in  
158 the outer margins of the pyrite-rich zone (Fig. 3B). Au precipitation is accompanied by a  
159 decrease in the concentration of Au bisulfide complexes (Fig. 3C).

160 The H<sub>2</sub> concentration in equilibrated model fluids decreases in cell 1 and  
161 increases slightly in the following cells; however, the concentration in each cell is always  
162 less than that in unreacted mixtures (Fig. 3D). This means that small amounts of H<sub>2</sub> are  
163 consumed during pyrite deposition.

164 The modeled concentration of graphite (C<sub>model</sub>) is the sum of graphite in the  
165 unreacted rock plus precipitated graphite (Fig. 3E). Precipitated graphite dominates  
166 C<sub>model</sub>, particularly in the first infiltration cell. Infiltrating CO<sub>2</sub> is reduced and precipitates  
167 as graphite. Inspection of the mineral modes allows deduction of the amount of CO<sub>2</sub> that  
168 is reduced (RE) to form graphite (CO<sub>2,RE</sub>) via

$$169 \quad \text{CO}_{2,\text{RE}(\text{aq})} = \text{CO}_{2,\text{lost}} - \text{CO}_{2,\text{carbonates}}, \quad (3)$$

170 where CO<sub>2,lost</sub> is the CO<sub>2</sub> lost from solution and CO<sub>2,carbonates</sub> is the CO<sub>2</sub> deposited as  
171 carbonate.

172 Graphite precipitation is also accompanied by a decrease in the CH<sub>4</sub> concentration  
173 in the fluid (CH<sub>4,RE</sub>) (Fig. 3E). CO<sub>2,RE</sub> and CH<sub>4,RE</sub> account for 51%–53% and 47%–49%  
174 of precipitated graphite, respectively. Model results at higher and lower temperatures  
175 show the same features (Table DR4).

## 176 **DISCUSSION AND CONCLUSIONS**

### 177 **Consistency of Rocks with Model Results**

178 Primary trends in mineralized natural rocks are replicated by the model. These  
179 include the increase in S and NCC contents (Fig. 2), syndepositional pyrite and graphite  
180 (Figs. 1C and 1D), and arsenopyrite peripheral to pyrite (Fig. 1). Features not replicated  
181 by the model, such as the late pyrite and arsenopyrite that overprints graphitic  
182 microshears (Figs. 1A and 1B), are texturally late and attributed to later fluid flow events,

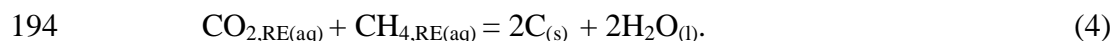


183 and the fact that mineralization is caused by infiltration of multiple fluids with different  
184 compositions rather than a monotonous single fluid infiltration event (Large et al., 2012).

### 185 **Precipitation of Sulfides**

186 The modeled coprecipitation of Au, sulfides, and graphite is most consistent with  
187 hypothesis 3 herein. Further information can be gained by an exploration of the electron  
188 transfer processes that form pyrite, graphite, and Au from aqueous  $\text{Au}^+$  in Au bisulfide,  
189  $\text{C}^{4+}$  in  $\text{CO}_{2,\text{RE}}$ ,  $\text{C}^{4-}$  in  $\text{CH}_{4,\text{RE}}$ , and from  $\text{S}^{2-}$  in bisulfide and  $\text{H}_2\text{S}$ .

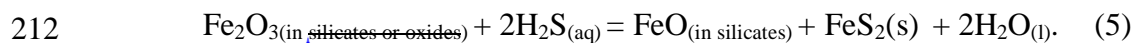
190 The most obvious change in fluid composition during fluid infiltration is a drop in  
191  $\text{CO}_{2,\text{RE}}$  and  $\text{CH}_{4,\text{RE}}$  concentrations that coincides with graphite deposition. Transfer of  
192 electrons between  $\text{CO}_{2,\text{RE}}$  and  $\text{CH}_{4,\text{RE}}$  forms water and graphite via Reaction 4 (e.g.,  
193 Ohmoto and Kerrick, 1977):



195 Calculated changes in modeled species abundances indicate that this reaction  
196 accounts for 94%–98% of precipitated graphite, with >90% of the  $\text{CO}_2$  and  $\text{CH}_4$  carried  
197 into the host rock by the ore fluids. However, the drop in  $\text{CO}_{2,\text{RE}}$  concentration is larger  
198 than that of  $\text{CH}_{4,\text{RE}}$ , indicating that more  $\text{CO}_{2,\text{RE}}$  than  $\text{CH}_{4,\text{RE}}$  is involved in fluid:rock  
199 reaction. Of the graphite that formed by  $\text{CO}_{2,\text{RE}}$  consumption, 2%–6% is not balanced by  
200  $\text{CH}_{4,\text{RE}}$  consumption and requires additional electrons. To investigate the electron transfer  
201 processes that formed this additional graphite, the precipitated graphite was split into two  
202 components:  $\text{C}_{\text{model1}}$ , graphite that can be accounted for by Reaction 4, and  $\text{C}_{\text{model2}}$ ,  
203 graphite that cannot be accounted for by Reaction 4.

204 Formation of pyrite from  $\text{H}_2\text{S}$  in solution requires an electron acceptor because  
205 divalent  $\text{S}^{2-}$  loses electrons to become monovalent  $\text{S}^-$  in pyrite. In light of the  $\text{CO}_{2,\text{RE}}$ -

206 CH<sub>4,RE</sub> imbalance discussed here, CO<sub>2,RE</sub> is a possible electron acceptor in the modeled  
207 system. The S<sub>model</sub>:C<sub>model2</sub> ratio was calculated, because if CO<sub>2,RE</sub> provides the electron  
208 acceptor for H<sub>2</sub>S-hosted sulfur, then pyrite and C<sub>model2</sub> should be correlated. The  
209 S<sub>model</sub>:C<sub>model2</sub> mass ratio is ~10 in all cells, which corresponds to a molar ratio of 4, as  
210 predicted by Reaction 2. Additional S deposition could be driven by transfer of electron  
211 to iron, e.g., via



213 Other electron transfer reactions can be written that involve H<sub>2</sub> and O<sub>2</sub>. However,  
214 the concentrations of these species in the model fluids are sufficiently low that such  
215 reactions could not contribute significantly to the redox budget of the mineralization  
216 process.

217 In natural systems, a combination of reactions such as Reactions 2, 4, and 5  
218 operate during time-integrated fluid flow to produce the observed S and NCC  
219 concentrations and petrography. The extent of progress of each reaction would depend on  
220 the microenvironment of mineralization in each rock, so the scattered natural data could  
221 be produced by a continuum between rocks in which reactions such as Reaction 2  
222 dominated sulfide deposition and those in which reactions such as Reaction 4 dominated  
223 graphite deposition (Fig. 2). Fluid infiltration prior to and post-Au mineralization, as well  
224 as progress of Reaction 5 and premetamorphic sulfide and CM in the natural rocks,  
225 would further alter S and NCC concentrations, so scattered natural data are expected.

## 226 **Gold Precipitation**

227 The model results suggest that the coexistence of CM and pyrite, often observed  
228 in natural samples, may be a consequence of their codeposition from sediment-derived

229 fluids, with a minor proportion of CM originally in situ in the host rocks. Deposition of  
230 pyrite and CM in the model is accompanied by gold precipitation (Fig. 3C). Au in the  
231 model is transported by the gold bisulfide complexes  $\text{Au}(\text{HS})^0$  and  $\text{Au}(\text{HS})_2^-$ . Decrease of  
232  $\text{H}_2\text{S}$  in the ore fluid drives destabilization of Au bisulfide complexes and causes gold  
233 precipitation (e.g., Seward, 1973). This model uses a sediment-derived ore fluid, as  
234 suggested by Large et al. (2011), and produces results consistent with observations.  
235 However, alternative sources of fluid, such as magmatic fluids, are not excluded by the  
236 model.

### 237 **Implications for Other Gold Deposits**

238 To summarize, most CM is proposed to be hydrothermal, and the primary role of  
239 carbon is as  $\text{CO}_2$ , to accept electrons from aqueous  $\text{H}_2\text{S}$  via Reaction 2. Consequent  
240 deposition of CM and pyrite decreases dissolved  $\text{H}_2\text{S}$  concentrations and destabilizes  
241 aqueous gold bisulfide complexes. At deposits such as Telfer in Australia, and Carlin in  
242 the United States, where host rocks are carbonate rich, decarbonation may provide an  
243 additional source of  $\text{CO}_2$  (Cline et al., 2005; Goellnicht et al., 1989), so the concepts  
244 presented here are only partially applicable to such deposits. However, the results  
245 presented here are broadly applicable to sediment-hosted orogenic gold deposits globally,  
246 although details, such as the spatial relationships and relative modes of arsenopyrite and  
247 the inferred importance of fluid immiscibility, may vary.

### 248 **ACKNOWLEDGMENTS**

249 We acknowledge the Commonwealth Scientific and Industrial Research  
250 Organisation (CSIRO) Flagship Collaboration Fund Cluster for Organic Geochemistry of  
251 Mineral Systems led by Curtin University (Australia), and the Western Australia Organic

252 and Isotope Geochemistry Centre, the Institute of Geoscience Research, Oceanagold  
253 Corporation, and the Ministry of Business, Innovation and Employment, New Zealand,  
254 for additional support. Hu acknowledges the receipt of Chinese Scholarship Council–  
255 Curtin International Postgraduate Research Scholarship, CSIRO Top-up Scholarship. We  
256 thank Andrew Tomkins, Iain Pitcairn, Jamie Wilkinson, Ross Large, and two anonymous  
257 reviewers for constructive reviews that greatly improved the manuscript.

## 258 REFERENCES CITED

- 259 Berge, J., 2011, Paleoproterozoic, turbidite-hosted, gold deposits of the Ashanti gold belt  
260 (Ghana, West Africa): Comparative analysis of turbidite-hosted gold deposits and an  
261 updated genetic model: *Ore Geology Reviews*, v. 39, p. 91–100,  
262 doi:10.1016/j.oregeorev.2010.12.001.
- 263 Bierlein, F.P., and Smith, P.K., 2003, The Touquoy Zone deposit: An example of  
264 “unusual” orogenic gold mineralisation in the Meguma terrane, Nova Scotia,  
265 Canada: *Canadian Journal of Earth Sciences*, v. 40, p. 447–466, doi:10.1139/e03-  
266 002.
- 267 Bierlein, F.P., Cartwright, I., and McKnight, S., 2001, The role of carbonaceous  
268 “indicator” slates in the genesis of lode gold mineralization in the Western Lachlan  
269 Orogen, Victoria, Southeastern Australia: *Economic Geology*, v. 96, p. 431–451,  
270 doi:10.2113/gsecongeo.96.3.431.
- 271 Cline, J.S., Hofstra, A.H., Muntean, J.L., Tosdal, R.M., and Hickey, K.A., 2005, Carlin-  
272 type gold deposits in Nevada: Critical geologic characteristics and viable models:  
273 *Economic Geology*, v. 100, p. 451–484, doi:10.5382/AV100.15.

- 274 Cox, S., Sun, S., Etheridge, M., Wall, V., and Potter, T., 1995, Structural and  
275 geochemical controls on the development of turbidite-hosted gold quartz vein  
276 deposits, Wattle Gully mine, central Victoria, Australia: *Economic Geology*, v. 90,  
277 p. 1722–1746, doi:10.2113/gsecongeo.90.6.1722.
- 278 Craw, D., 2002, Geochemistry of late metamorphic hydrothermal alteration and  
279 graphitisation of host rock, Macraes gold mine, Otago Schist, New Zealand:  
280 *Chemical Geology*, v. 191, p. 257–275, doi:10.1016/S0009-2541(02)00139-0.
- 281 Craw, D., Mortensen, J., MacKenzie, D., and Pitcairn, I., 2015, Contrasting geochemistry  
282 of orogenic gold deposits in Yukon, Canada and Otago, New Zealand: *Geochemistry*  
283 *Exploration Environment Analysis*, v. 15, p. 150–166, doi:10.1144/geochem2013-  
284 262.
- 285 De Ronde, C.E., Faure, K., Bray, C.J., and Whitford, D.J., 2000, Round Hill shear zone–  
286 hosted gold deposit, Macraes Flat, Otago, New Zealand: Evidence of a magmatic ore  
287 fluid: *Economic Geology*, v. 95, p. 1025–1048, doi:10.2113/gsecongeo.95.5.1025.
- 288 Goellnicht, N., Groves, D., McNaughton, N., and Dimo, G., 1989, An epigenetic origin  
289 for the Telfer gold deposit, Western Australia, *in* Keays, R.R., et al., eds., *The*  
290 *geology of gold deposits: The perspective in 1988: Economic Geology*  
291 *Monograph 6*, p. 151–167, doi:10.5382/Mono.06.11.
- 292 Goldfarb, R.J., and Groves, D.I., 2015, Orogenic gold: Common or evolving fluid and  
293 metal sources through time: *Lithos*, v. 233, p. 2–26,  
294 doi:10.1016/j.lithos.2015.07.011.
- 295 Henne, A., and Craw, D., 2012, Synmetamorphic carbon mobility and graphite  
296 enrichment in metaturbidites as a precursor to orogenic gold mineralization, Otago

- 297 Schist, New Zealand: *Mineralium Deposita*, v. 47, p. 781–797, doi:10.1007/s00126-  
298 012-0399-2.
- 299 Hu, S., Evans, K., Craw, D., Rempel, K., Bourdet, J., Dick, J., and Grice, K., 2015,  
300 Raman characterization of carbonaceous material in the Macraes orogenic gold  
301 deposit and metasedimentary host rocks, New Zealand: *Ore Geology Reviews*, v. 70,  
302 p. 80–95, doi:10.1016/j.oregeorev.2015.03.021.
- 303 Hu, S.-Y., Evans, K., Fisher, L., Rempel, K., Craw, D., Evans, N.J., Cumberland, S.,  
304 Robert, A., and Grice, K., 2016, Associations between sulfides, carbonaceous  
305 material, gold and other trace elements in polyframboids: Implications for the source  
306 of orogenic gold deposits, Otago Schist, New Zealand: *Geochimica et*  
307 *Cosmochimica Acta*, v. 180, p. 197–213, doi:10.1016/j.gca.2016.02.021.
- 308 Křibek, B., Sýkorová, I., Machovič, V., Kněsl, I., Laufek, F., and Zachariáš, J., 2015, The  
309 origin and hydrothermal mobilization of carbonaceous matter associated with  
310 Paleoproterozoic orogenic-type gold deposits of West Africa: *Precambrian Research*,  
311 v. 270, p. 300–317, doi:10.1016/j.precamres.2015.09.017.
- 312 Large, R.R., Bull, S.W., and Maslennikov, V.V., 2011, A carbonaceous sedimentary  
313 source-rock model for Carlin-type and orogenic gold deposits: *Economic Geology*,  
314 v. 106, p. 331–358, doi:10.2113/econgeo.106.3.331.
- 315 Large, R., Thomas, H., Craw, D., Henne, A., and Henderson, S., 2012, Diagenetic pyrite  
316 as a source for metals in orogenic gold deposits, Otago Schist, New Zealand: *New*  
317 *Zealand Journal of Geology and Geophysics*, v. 55, p. 137–149,  
318 doi:10.1080/00288306.2012.682282.

- 319 Ohmoto, H., and Kerrick, D., 1977, Devolatilization equilibria in graphitic systems:  
320 American Journal of Science, v. 277, p. 1013–1044, doi:10.2475/ajs.277.8.1013.
- 321 Petrie, B., Craw, D., and Ryan, C., 2005, Geological controls on refractory ore in an  
322 orogenic gold deposit, Macraes mine, New Zealand: Mineralium Deposita, v. 40,  
323 p. 45–58, doi:10.1007/s00126-005-0467-y.
- 324 Pitcairn, I.K., Roberts, S., Teagle, D.A., and Craw, D., 2005, Detecting hydrothermal  
325 graphite deposition during metamorphism and gold mineralization: Journal of the  
326 Geological Society [London], v. 162, p. 429–432, doi:10.1144/0016-764904-139.
- 327 Pitcairn, I.K., Teagle, D.A., Craw, D., Olivo, G.R., Kerrich, R., and Brewer, T.S., 2006,  
328 Sources of metals and fluids in orogenic gold deposits: Insights from the Otago and  
329 Alpine Schists, New Zealand: Economic Geology, v. 101, p. 1525–1546,  
330 doi:10.2113/gsecongeo.101.8.1525.
- 331 Seward, T.M., 1973, Thio complexes of gold and the transport of gold in hydrothermal  
332 ore solutions: Geochimica et Cosmochimica Acta, v. 37, p. 379–399,  
333 doi:10.1016/0016-7037(73)90207-X.
- 334 Shvarov, Y.V., and Bastrakov, E., 1999, HCh: A software package for geochemical  
335 equilibrium modelling: User's guide: Australian Geological Survey Organisation,  
336 Science and Resources Record, v. 25, p. 61.
- 337 Thomas, H.V., Large, R.R., Bull, S.W., Maslennikov, V., Berry, R.F., Fraser, R., Froud,  
338 S., and Moye, R., 2011, Pyrite and pyrrhotite textures and composition in sediments,  
339 laminated quartz veins, and reefs at Bendigo gold mine, Australia: Insights for ore  
340 genesis: Economic Geology, v. 106, p. 1–31, doi:10.2113/econgeo.106.1.1.

341 Tomkins, A.G., 2010, Windows of metamorphic sulfur liberation in the crust:  
342 Implications for gold deposit genesis: *Geochimica et Cosmochimica Acta*, v. 74,  
343 p. 3246–3259, doi:10.1016/j.gca.2010.03.003.

344 Upton, P., and Craw, D., 2008, Modelling the role of graphite in development of a  
345 mineralized mid-crustal shear zone, Macraes mine, New Zealand: *Earth and*  
346 *Planetary Science Letters*, v. 266, p. 245–255, doi:10.1016/j.epsl.2007.10.048.

347 **FIGURE CAPTIONS**

348 Figure 1. Photomicrographs of gold-bearing sulfides from the Macraes deposit (New  
349 Zealand). A: Transmitted light image of pyrite (circled by dashed lines) surrounded by  
350 graphitic shears (dotted lines) that contain fine-grained carbonaceous material (CM) and  
351 sulfides, especially arsenopyrite. B: Backscattered electron (BSE) image of pyrite  
352 surrounded by graphitic shears. Pyrite is light gray and arsenopyrite is white. C:  
353 Transmitted light image of pyrite overprinting graphitic shears. D: BSE image of pyrite  
354 overprinting graphitic shears.

355

356 Figure 2. Sulfur (S) versus noncarbonate carbon (NCC) by mass from four goldfields  
357 compared to model results. A vector from unmineralized rock to cell 1 is used to indicate  
358 the modeled trajectory in S versus NCC space. This vector can be considered as the sum  
359 of a vector that represents graphite deposition via Reaction 4 (R 4), and a vector toward  
360 high  $S_{\text{model}}:C_{\text{model}}$  ratios via sulfide deposition (Reaction 2, R 2).

361

362



363 Figure 3. Results of fluid infiltration at 220 °C, 3 kbar. In cell 0, the concentration of  
364 solid components represents the amount in unreacted GB-01 and that of aqueous  
365 components represents the total amount in unreacted country-rock fluid or ore fluid.  
366 Results of the fluid infiltration are presented in cells 1–14. A: Pyrite and pyrrhotite. B:  
367 Arsenopyrite. C: Au and Au bisulfide species. D: H<sub>2</sub> in equilibrated fluids and unreacted  
368 mixtures. E: Total graphite (C<sub>model</sub>), precipitated graphite, CH<sub>4,RE</sub>, and CO<sub>2,RE</sub> (see text).

369

370

371 <sup>1</sup>GSA Data Repository item 2017xxx, xxxxxxxx, is available online at  
372 <http://www.geosociety.org/pubs/ft2017.htm> or on request from [editing@geosociety.org](mailto:editing@geosociety.org).